A hybrid micro-ECoG for functionally targeted multi-site and multi-scale investigation

Patrick Jendritza[1,2*], Rickard Liljemalm[3], Thomas Stieglitz[3], Pascal Fries[1,2,4], and Christopher Murphy Lewis[1,5*]

[1]Ernst Strüngmann Institute (ESI) for Neuroscience in Cooperation with Max Planck Society, Deutschordenstraße 46, 60528 Frankfurt, Germany

[2]International Max Planck Research School for Neural Circuits, Max-von-Laue-Straße 4, 60438 Frankfurt, Germany

[3]Laboratory for Biomedical Microtechnology, Department of Microsystems Engineering (IMTEK), BrainLinks-BrainTools Center and the Bernstein Center Freiburg, Albert-Ludwigs-Universität Freiburg, 79110 Freiburg, Germany

[4]Max Planck Institute for Biological Cybernetics, Max-Planck-Ring 8, 72076 Tübingen, Germany

[5]Brain Research Institute, University of Zurich, Winterthurerstrasse 190, 8057 Zurich, Switzerland

[*]Correspondence: pjendritza@salk.edu (P.J.) and lewis@hifo.uzh.ch (C.M.L.)

Summary

Brain function relies on the coordination of activity across a wide range of spatial and temporal scales. The activity of single neurons depends on their unique pattern of local and long-range connectivity and thus on the coordination of local activity with large-scale patterns of distributed activity across brain-wide networks. Understanding integrated, whole brain function requires new tools capable of recording from anatomically connected populations in distributed brain areas to bridge local and global dynamics. Here, we present high-density, micro-electrocorticography arrays that facilitate multi-scale studies of brain activity. The arrays are hybrid designs that integrate the desirable features of silicone elastomers and polyimide films. The silicone elastomer superstructure provides optical transparency and permits repeated mechanical penetration with rigid linear electrode arrays. The polyimide films provide the capacity for fine feature definition through photolithography. This combination facilitates high-throughput functional mapping of areas of interest to target functionally characterized populations for refined, dense sampling. We demonstrate the suitability of the technique for functional mapping of cortical regions in rats, cats and marmosets and the benefit of the resulting functional maps for targeting functionally defined populations for dense, multi-area laminar recordings. Finally, we demonstrate the utility of the hybrid μECoG to localize optogenetically evoked feedforward excitation in down-stream cortical regions to investigate cortico-cortical interactions. Together, these capabilities make the hybrid μECoG a compelling tool for systems neuroscience.

Introduction

The introduction of new optical and electrophysiological tools, as well as the widespread adoption of functional brain imaging, has prompted a paradigm shift in systems neuroscience away from a focus on individual neurons and brain areas and towards a greater appreciation of coordinated activity across brain-wide networks.[1–10] While classic studies focused on the functional characterization of single neurons and brain areas,[11–14] advances over the past decades have demonstrated the importance of understanding the coordination of neuronal populations within local microcircuits and the integration of activity across distributed, brain-wide networks.[15–19] Indeed, while neurons are powerful computational units,[20–22] the brain's remarkable capabilities are achieved through communication within and between neuronal groups, and the functional characteristics of single neurons can be better understood in light of local and global activity patterns.[18,23–25] These insights have been critically aided by methodological advances that enable multi-scale and multi-modal measurement and perturbation of brain activity[7,15,16,26,27] to map

neuronal activity both densely within a local microcircuit and broadly, across relevant brain regions. However, to date, our understanding of distributed processing in the brain is fundamentally limited by our ability to record simultaneously from multiple, anatomically connected neuronal populations across brain-wide networks with high spatial and temporal precision.

Currently, simultaneous inter-areal recordings of communicating neurons require the laborious search for functionally paired locations in areas of interest guided by anatomy or based on functional maps determined using imaging in different experimental sessions. The difficulty of localizing the specific subpopulations of anatomically connected, communicating neurons, especially in large brains, has hampered the investigation of inter-areal communication, particularly at the cellular scale.[28,29] New tools and techniques are required to investigate the principles of multi-scale brain activity that bridge cellular activity within local circuits to distributed patterns of activity across brain-wide networks.[30,31] The rapid development of optical methods to functionally image populations of neurons[7,32,33] in combination with viral and genetic methods to target specific neuron classes based on their cell-type or their pattern of inter-areal axonal projections[34–36] have made it possible to monitor specific projection neurons and functionally characterize the axons or somata of projecting cells in a directed manner.[37–39] However the field-of-view of most microscopes is still limited to imaging one local population (but see: [40–42]), and population imaging does not yet permit the reliable recording of single action potentials at the millisecond temporal scale. In parallel, advances in the design and fabrication of intracortical multielectrode arrays have greatly increased the number and density of recording sites, permitting high-yield recordings of neuronal activity within areas of interest.[43,44] However, it is difficult to scale the placement of multiple multielectrode arrays to cover brain-wide networks for simultaneous recording (but see: [45,46]). In contrast, micro-electrocorticography (μECoG) provides a means to record from distributed brain regions with broad coverage and high spatial and temporal resolution, but it is limited to signals at the surface of the brain.[47–49] The complementary features of these two approaches offer a compelling combination: functional maps derived from the large-scale, high-resolution mapping afforded by μECoG can be used to specify candidate targets for dense local sampling across the cortical depth with intracortical multi-electrode arrays[50,51]. Functional mapping and targeted recording can be combined across brain areas, where functional topography partially determines the likelihood of communicating subpopulations, thereby increasing the probability of recording from anatomically connected neuronal populations and aiding the investigation of inter-areal communication.[52,53] This is particularly the case for

areas with clear functional topography, such as retinotopically organized areas of the visual cortex[54], tonotopically organized areas of the auditory cortex[55], or somatotopically organized regions of the somatosensory and motor cortex.[56,57]

We present a hybrid μECoG for performing large-scale, high-resolution functional characterization of targeted brain areas in combination with dense, functionally targeted local sampling from regions of interest. The combination of high-resolution multi-electrode arrays fabricated on polyimide thin-films with transparent, flexible and elastic silicone elastomers (Polydimethylsiloxane, PDMS) enables high-resolution electrical sampling from the cortical surface, while preserving optical access to the underlying cortex. Further, the flexibility, elasticity and self-sealing nature of PDMS permits repeated penetration with rigid linear arrays to perform recordings of neuronal activity across the cortical depth in functionally identified populations.[58,59] The hybrid μECoGs are conformal[60] to the delicate cortical surface and provide dense functional information spanning large regions of interest at the scale of cortical areas (tens to hundreds of square millimeters). We demonstrate the utility of the design in three different species (rat, cat, and marmoset) and show that the arrays are capable of recording both the low frequency, local field potential, as well as the aggregate spiking activity of superficial neurons recorded from the cortical surface.[49] These signals can be used to functionally characterize the local population across the cortical surface, enabling the targeting of specific populations for depth recordings with multielectrode arrays inserted into the brain while the μECoG remains in place. We further show that the optical transparency of the hybrid μECoG permits local and inter-areal activation using optogenetics.[61] This approach enables the investigation of local circuit activity in relation to ongoing, large-scale, multi-area brain states, as well as interference with functionally characterized populations and optogenetic activation of inter-areal projection neurons. Such tools promise to open new avenues for investigating the integration of cellular activity with whole-brain activity patterns.

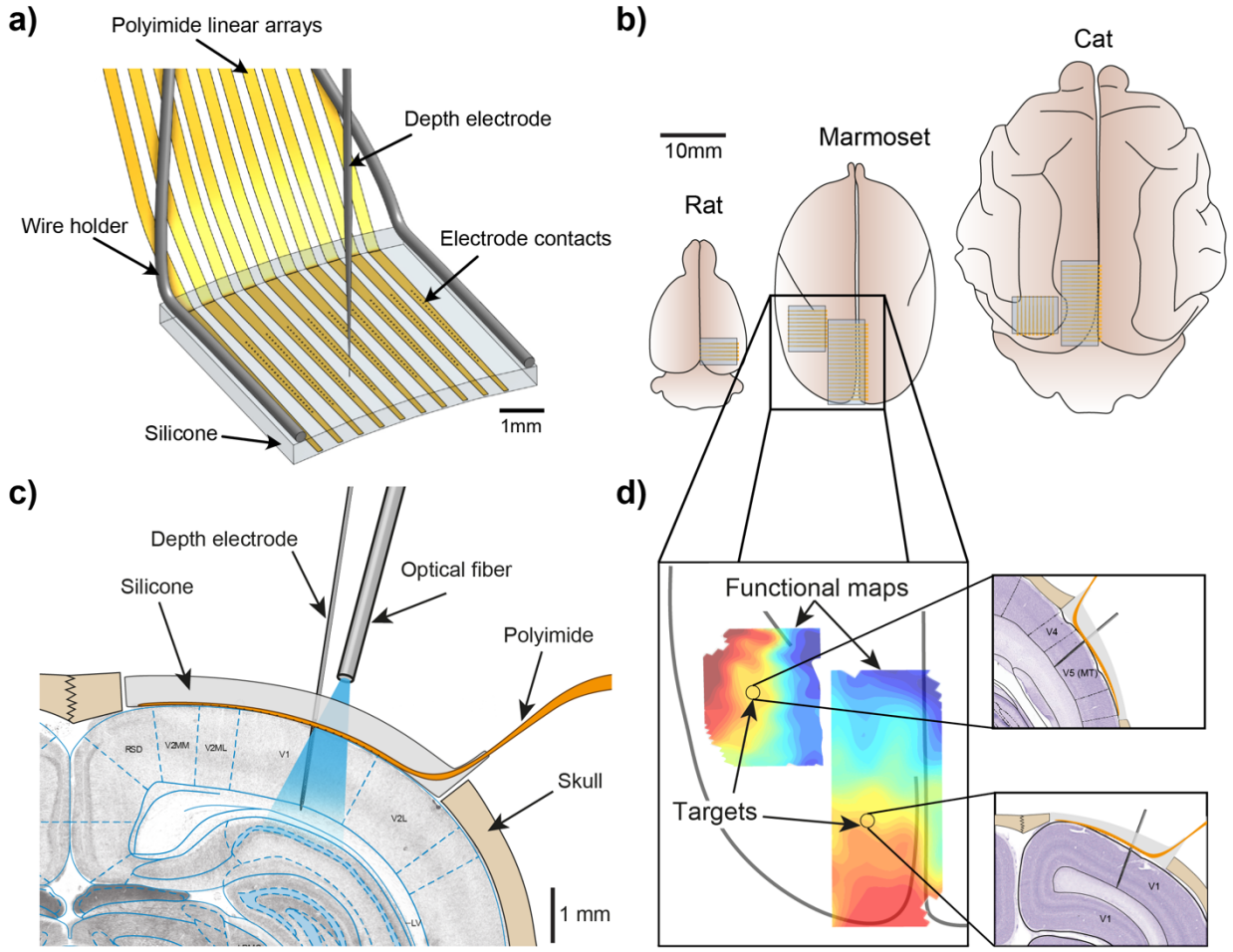

Figure 1: A hybrid μECoG for functionally targeted, multi-scale investigation. a) Illustration of a 240-channel hybrid μECoG array showing ten 24-electrode polyimide thin-film linear electrode arrays regularly arranged and encapsulated in a silicone elastomer and secured to a wire holder for placement on the brain. A depth electrode is depicted penetrating the hybrid μECoG at a desired location. **b)** Illustration of hybrid μECoG arrays placed on the rat, marmoset and cat brain to indicate the scale of recordings and coverage of different array designs on the model organisms used in this study. **c)** Schematic of a hybrid μECoG in place on the rat brain with a penetrating linear depth array and an optical fiber to perform optogenetic activation of local neurons or projections. **d)** Schematic illustration of hypothetical functional maps derived from μECoG recordings from the cortical surface and hypothetical target locations picked by similarity of functional maps. (Right) Illustration of depth linear electrode arrays inserted through the μECoG to record laminarly resolved neuronal activity from the target locations in the marmoset brain.

Results

A hybrid µECoG for functionally targeted multi-scale investigation

We developed a hybrid µECoG array to enable high-resolution functional characterization of brain areas from the cortical surface, while permitting combined recordings with depth electrodes and optical access for optogenetic perturbations or imaging. High resolution is realized by flexible linear electrode arrays fabricated through photolithography on polyimide thin films, while optical and depth access are provided by a superstructure formed from silicone elastomer (Figure 1a). Silicone elastomers provide a few other practical advantages over a pure thin-film ECoG array. Silicone is soft and conformal, gently accommodating to the cortical surface, avoiding edema and sealing the exposed cortex, while avoiding wrinkling or buckling which would be difficult or impossible to achieve with the polyimide alone. Once fabricated, the polyimide linear arrays can be easily and flexibly assembled to match the size of specific brain areas or the brains of different species. To illustrate the flexibility and utility of these arrays, we assembled different configurations and used them to map the retinotopy of visual cortical areas and investigate local and inter-areal interactions across the visual cortical hierarchy of three model systems: the rat, the marmoset and the cat (Figure 1b). The arrays can be configured to have higher or lower recording density depending on needs and can be flexibly positioned to record from brain areas of interest. Once in place on the cortical surface, the hybrid µECoG allows repeated penetration with depth electrodes and provides optical access for simultaneous optogenetic stimulation, or imaging (Figure 1c). To target populations of interest, or to increase the chances of recording subpopulations of anatomically connected neurons, functional maps can be estimated from the µECoG recordings, and sites of interest with similar tuning or response properties can be selected for simultaneous laminar recording with penetrating linear arrays (Figure 1d). We introduce the fabrication of hybrid µECoG arrays and illustrate their utility for investigating local and inter-areal cortical interactions in the visual system of anesthetized rats, cats, and marmosets.

Fabrication of a hybrid µECoG

We fabricated µECoG arrays in a two-step process, using two biocompatible polymers to produce a hybrid array that combines the complementary advantages of each. First, Micro-Electro Mechanical Systems (MEMS) processes were used to fabricate flexible high-density linear electrode arrays on polyimide thin films (Fig 2A).[47,62–64] MEMS fabrication with polyimide permits small feature sizes, flexibility and biocompatibility, but polyimide is not transparent, has some autofluorescence, and cannot be penetrated by sharp electrodes. To achieve the desired

151 features, these high-density polyimide arrays were integrated into a silicone elastomer
152 (Polydimethylsiloxane, PDMS) that can act as a dural replacement, is optically transparent,
153 stretchable and flexible and can be repeatedly penetrated by sharp electrodes (Fig 2B).[50,65,66]
154 However, in contrast to polyimide, it is challenging to achieve high-resolution, small features on
155 PDMS using standard MEMs fabrication processes, because of its elasticity and poor adhesion
156 with photoresist. In addition, PDMS is not compatible with standard MEMS cleanroom
157 manufacturing since residues contaminate machines and surfaces and seriously deteriorate
158 process performance. Using this two-step process also permitted us to decouple the precision
159 lithography necessary to fabricate high-density arrays, from the modular assembly of multiple
160 thin-film arrays into the final hybrid μECoG. By using this two-step process, a single thin-film
161 design can be recombined into multiple μECoG arrangements that can be assembled in the lab,
162 without the need for further work in the clean room. The μECoG can thus be flexibly assembled
163 to match the geometry of the brain area and species of choice and reassembled for different
164 experiments, eliminating the need for costly photolithography mask redesigns and other time-
165 intensive cleanroom procedures.

166 In this process, the design of the high-resolution thin-film electrode arrays is the first step, and it
167 is desirable to choose a layout that can be flexibly integrated into different hybrid μEcoG
168 configurations in a modular fashion. To maximize modularity, we designed two linear electrode
169 layouts for this study (10 μm thickness), one with 12 contacts spaced by 0.2 mm and the other
170 with 24 contacts spaced by 0.15 mm, and both with circular, 35 μm diameter platinum recording
171 sites (Figure 2c). Standard cleanroom fabrication processes were used to structure conductive
172 elements on polyimide thin-films using photolithography, resulting in smaller electrodes, traces
173 and higher electrode densities than can be fabricated directly on silicone elastomers[47,67]. To
174 achieve a regular 2-dimensional arrangement of recording sites over our cortical sites of interest,
175 polyimide linear arrays were arranged in a regular planar layout on a glass slide and then attached
176 to the underside of a previously fabricated PDMS sheet (Figure 2d). The sheet (0.5-0.8 mm
177 thickness) was placed on top of the polyimide arrays, and PDMS was then applied to the front
178 and the back of the arrays (the locations where no electrode contacts were exposed) to attach
179 them securely to the sheet. Lastly, the metal wire holders were lowered onto the assembly with a
180 micromanipulator, and more PDMS was applied to attach the holders to the PDMS sheet. The
181 transparency of the assembled hybrid μECoG permitted visualization of the underlying brain and
182 of the epifluorescence from populations of cells expressing fluorescent reporters (Fig 2e). We
183 constructed three distinct hybrid μECoGs with different sizes and spatial densities of electrodes.

The first array had 0.15 mm electrode pitch and 0.55 mm strip pitch. It consisted of five linear array strips, each with 24 channels, resulting in a total of 120 electrode contacts and covering an area of 2.2 × 3.45 mm. The second array consisted of ten linear array strips with a pitch of 0.6 mm, each with 24 channels, resulting in a total of 240 electrode contacts and covering an area of 5.4 × 3.45 mm. The third array consisted of 20 linear array strips with a pitch of 0.6 mm, each with 12 channels, resulting in a total of 240 electrode contacts and covering an area of 11.4 × 2.2 mm. The hybrid µECoG designs permitted dense recording from visual cortical areas of the rat, cat and marmoset.

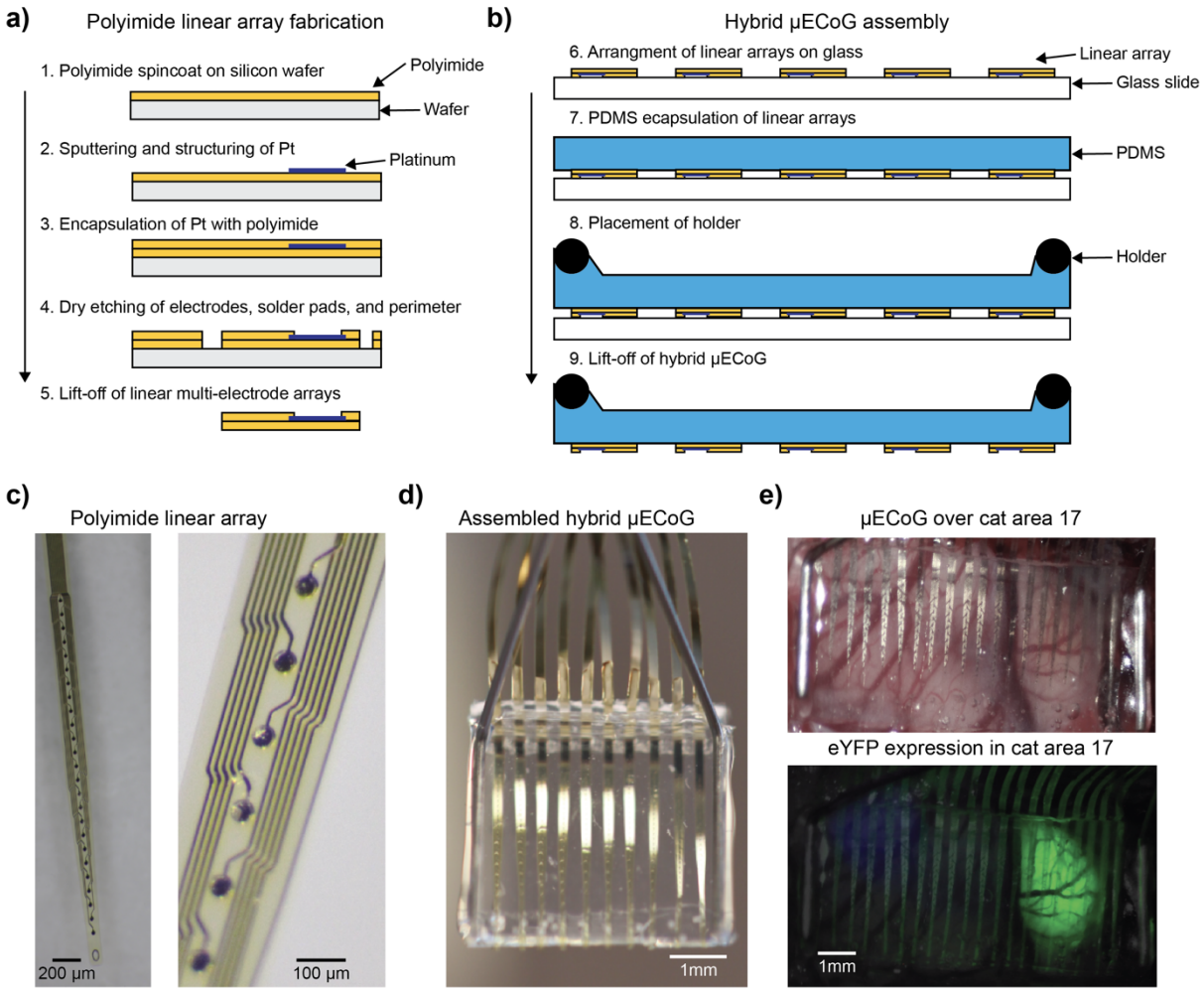

Figure 2: Fabrication of the hybrid µECoG. a) Illustration of the fabrication sequence for the polyimide thin-film electrode arrays. **b)** Illustration of the assembly of the hybrid µECoG by regular arrangement of polyimide thin-film arrays and encapsulation with silicone (PDMS) and attachment of the wire-holder. **c)** Photomicrographs of a 24-channel polyimide linear array with 35 µm diameter platinum electrode sites. **d)**

Photograph of an assembled hybrid μEcoG with ten 24-channel polyimide thin-film arrays. **e)** Photograph of a hybrid μECoG with twenty 12-channel polyimide thin-film arrays placed over the cat primary visual cortex (top), and epifluorescence image (bottom) showing the virally expressed fluorescence protein (eYFP).

Hybrid μECoGs record high-quality signals and permit functional mapping from the cortical surface

We first tested the hybrid μECoG in the visual system of the anesthetized cat and rat (Figure 3, cat and Figure S1, rat). The arrays were placed directly on the cortical surface after removal of the dura mater (Figure 3a, Figure S1b) and were able to reliably measure electrical activity from the cortical surface for multiple hours or days. Arrays could be removed and cleaned using detergent and were reusable in different experiments across months and years.

To demonstrate the utility of the hybrid μECoG for functional characterization of brain areas, we placed two hybrid μECoG arrays over two anatomically connected and retinotopically organized areas of the cat visual hierarchy. The visual system of the cat is arguably the prototypical system for investigating hierarchical cortical processing and laminar organization.[68–70] To perform large-scale functional characterization, we placed hybrid μECoG arrays over the primary visual cortex (V1, areas 17 and 18) and an intermediate area of the ventral visual stream (area 21a, a homologue of area V4 in the primate[71]). We placed one μECoG (20 x 12 electrodes with 0.2 by 0.6 mm spacing) over V1 and a second μECoG (10 x 24 electrodes with 0.15 by 0.6 mm spacing) over area 21a. We found that sites across the μECoG were visually responsive and could record both the aggregate spiking of multiple neurons (multi-unit activity (MUA), Figure 3b-d) and local field potential (LFP) or electroencephalogram (EEG) signals (Figure 3e) from the cortical surface in response to a full-field, full-contrast square-wave grating stimulus. We next performed visual receptive field mapping using a stimulus that consisted of a moving bar (white on black background) moving across the visual field in a random sequence of 16 different directions. Receptive fields could be estimated using either the MUA or the gamma-band LFP activity (Figure S1 for rat and S2 for cat) and resulted in highly consistent selectivity for recording sites (Figure 3f-g). The retinotopic position calculated from the receptive field centers produced functional maps that revealed the expected retinotopic organization of visual areas in the cat (Figure 3h). The visual receptive fields in area 21a appeared on average larger and moved more in visual space in a smaller amount of cortical space than those in area 17.

We next inserted intracortical microelectrodes through the PDMS portion of the hybrid μECoG, adjacent to the polyimide thin-film linear electrode arrays to perform simultaneous depth

recordings from functionally characterized neuronal populations, first with tungsten microelectrodes and subsequently with intracortical multi-electrode arrays. The retinotopic selectivity of neurons recorded with penetrating tungsten electrodes from the underlying cortex matched well with that expected based on the functional mapping with the hybrid μECoG (Figure S2b-c, right). This close correspondence enabled targeted recordings of functionally

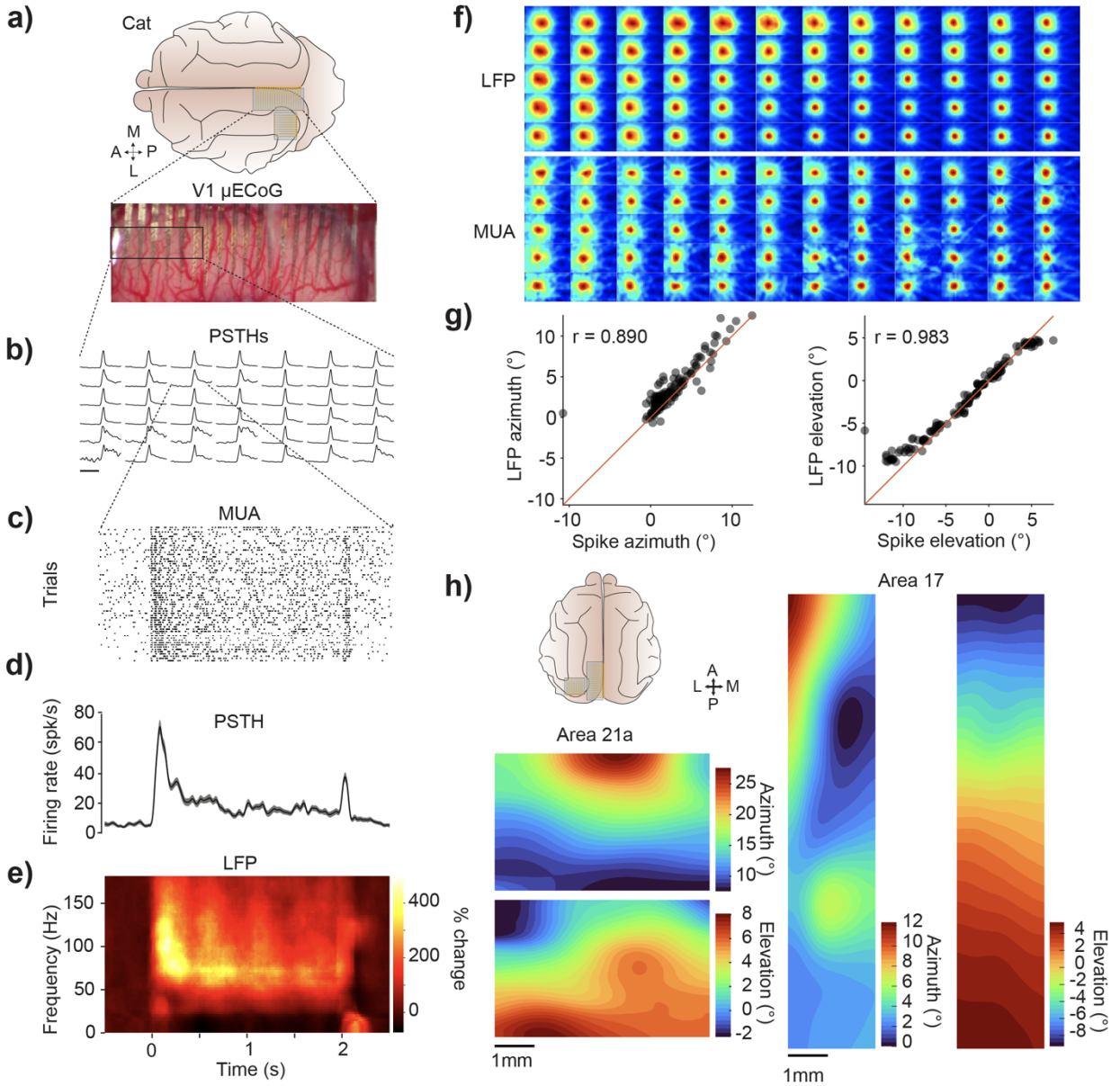

Figure 3: Hybrid μECoG enables dense, multi-scale functional mapping from LFP and MUA across the visual system in the anesthetized cat. a) Illustration of the experimental setup with two μECoG arrays over the cat visual cortex, and photograph of the array over cortical area 17. **b)** PSTHs of the average MUA for a subset of electrodes as indicated by the rectangle in the photograph above. Scale bar equals 500 ms. **c)** Raster plot showing individual MUA spikes detected on one example electrode for multiple trials of visual

stimulation. **d)** PSTH and **(e)** time-frequency plot for the full stimulus duration of two seconds. Shaded area in (d) indicates SEM. The x-axis in (e) applies to (c) through (e). The visual stimulus induced strong MUA and sustained gamma-band activity. **f)** Comparison of RFs mapped using gamma-band LFP power or MUA for the same electrode sites in areas 17. **g)** Correlation between the gamma-band LFP and MUA estimated RF center for the azimuth (left) and elevation (right). **h)** Retinotopic maps for cat areas 21a and 17 computed from the LFP-estimated RFs. Clear variation in the retinotopic position vary across the cortical areas as expected from single neuron recordings using repeated penetrations with single electrodes or fMRI.

characterized populations within an area of interest. Moreover, the placement of multiple µECoG arrays permitted the simultaneous mapping of visual space in area 17 and area 21a and the subsequent targeting of retinotopically overlapping neurons across the cortical depth simultaneously in both areas (Figure S2b-c). The functional map estimated with the µECoG allowed us to target portions of area 17 and 21a representing similar portions of visual space and likely to be anatomically connected.

Hybrid µECoGs enable multi-scale investigation of cortical activity

To demonstrate the capacity for multi-scale investigation of cortical activity patterns both topographically across the cortical surface, but also in the depth with laminar electrode arrays, we combined the surface recordings from the µEcoG in cat area 21a with a multi-shank laminar electrode array (Figure 4a). We inserted a 128-channel electrode array (Atlas Neurotech, 4 shanks with each 32 electrodes spaced by 100 µm) based on functional mapping at the desired retinotopic position at the medial edge of the µEcoG array (Figure 4b). The combined recording enables correlating the 2D surface signals from the µEcoG with the signals from the laminar array across all depths of the cortex. The topography of the resulting correlation values depended on the frequency band of the cortical activity, the depth along the laminar electrode array, as well as the position of the laminar electrode array relative to the µEcoG (Figure 4c). The correlation pattern from the high frequency activity (100-200 Hz) showed a singular localized spatial peak at the position closest to the corresponding laminar array (colored arrows in Figure 4c). Specifically, the correlation peak for shank 1 was located at the medial edge of the array, slightly posterior from the center, whereas the peak for shank 4 was located at the most posterior medial edge, as

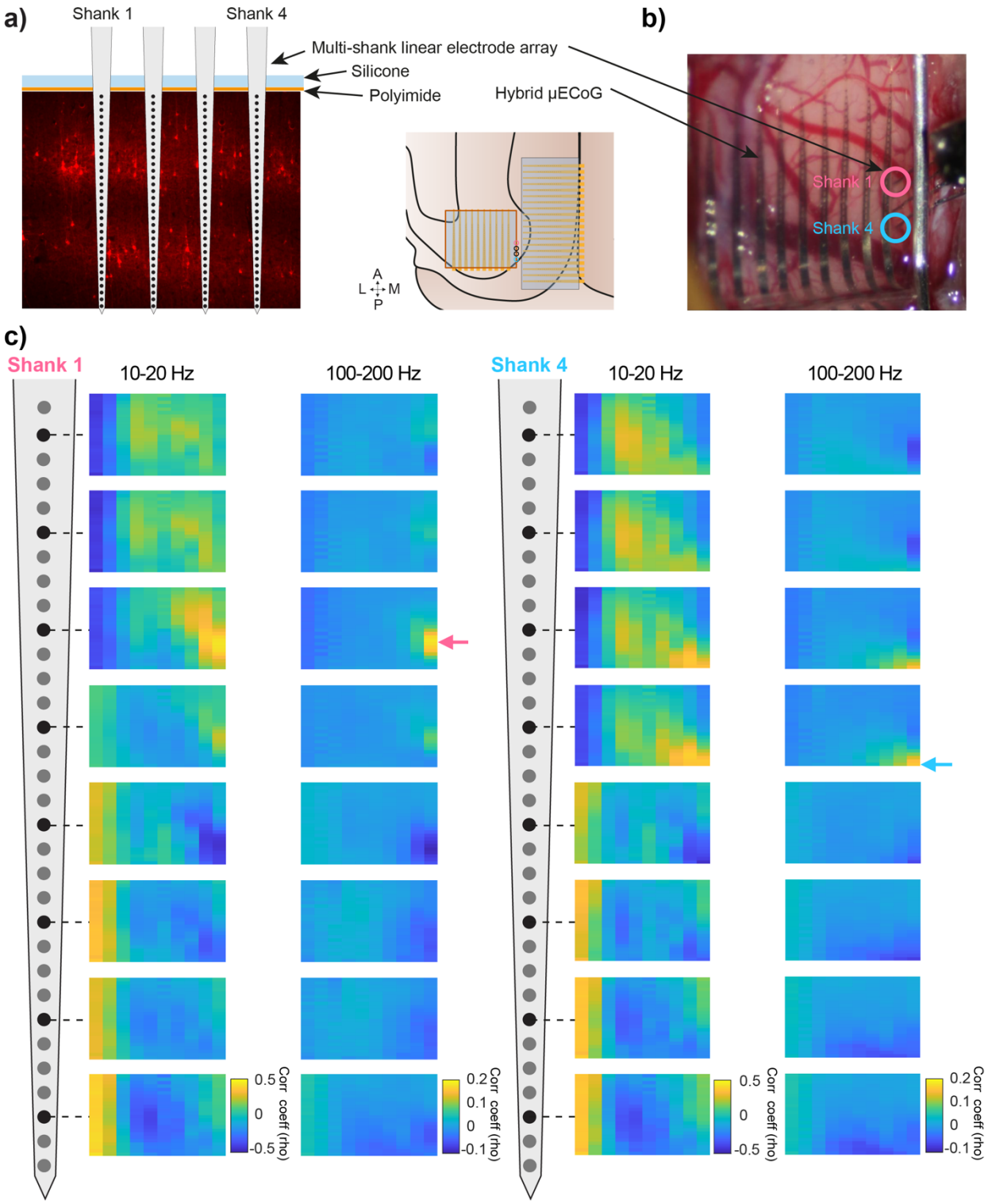

Figure 4: Hybrid µECoG enables investigation of multi-scale interactions between laminar and topographical activity patterns. a) Schematic illustration of a multi-shank laminar electrode array inserted at the edge of a hybrid µECoG in area 21a based on retinotopic functional mapping. **b)** Photograph of the high-density hybrid µECoG placed over area 21a with the inserted multi-shank laminar electrode array.

Circles indicate positions of shanks 1 and 4. **c)** Topographical pattern of correlation between two different shanks of the laminar array and the band-limited LFP in two frequency ranges showing differential 2D correlation patterns by frequency and depth. Note the singular localized spatial peak at the position closest to the corresponding laminar array.

expected from the location of the laminar arrays (Figure 4b). Interestingly, the sign of the localized correlation peaks flipped from positive to negative deeper in the brain. This reversal in correlation sign is consistent with the known reversal of the LFP across layers.[72] The correlation patterns from the low frequency LFP components (10-20Hz) resembled this pattern but it was less localized and showed larger absolute correlation values, as well as additional spatial features when compared to the high frequency patterns.

Hybrid μECoG for functionally targeted multi-area laminar recordings in the marmoset.

To aid the investigation of inter-areal interactions in the visual system, we next used the hybrid μECoG to map multiple areas in the visual hierarchy of the anesthetized marmoset. We placed two μECoG arrays over the primary visual cortex (V1) and an intermediate visual area (medial temporal area, MT/V5) to map their retinotopic organization. We then used the μECoG-derived retinotopic maps to guide the insertion of linear depth electrodes for functionally aligned multi-area laminar recordings (Figure 4a). As with the rat and cat, we were able to estimate visual receptive fields from the LFP and MUA recorded from the surface of the brain in the marmoset (Figure 4b). Receptive fields recorded from the laminar multi-electrode arrays inserted through the hybrid μECoG matched those of nearby electrodes on the μECoG array but not those of more distant electrodes (Figure 4b). This allowed simultaneous laminar recordings of targeted regions in areas V1 and MT of the marmoset. Simultaneous laminar and μECoG recordings permit activity across the cortical depth to be related to ongoing activity in local and distant cortical populations according to their functional correspondence (Figure 4c-d). Spiking activity recorded from the cortical depth also demonstrated the known orientation and direction selectivity of cortical columns in the primate and cat primary visual cortex (Figure 4e). Such an approach can greatly increase the efficiency of localizing functionally aligned populations for multi-area laminar recordings. Furthermore, simultaneous μECoG and laminar recordings allow the investigation of cortical interactions across spatial scales.

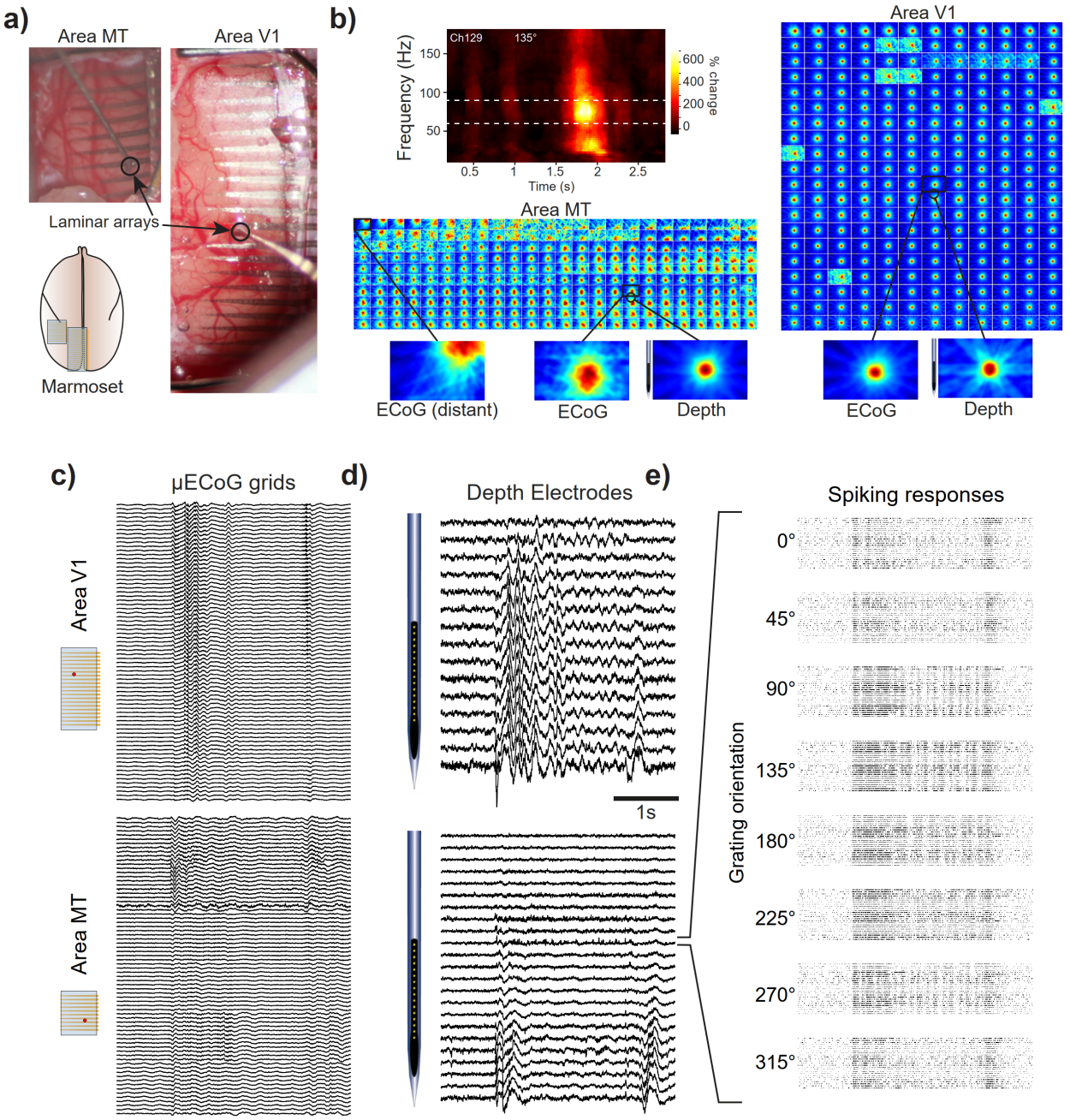

Figure 5: Hybrid μECoG enables functionally targeted multi-area laminar recordings in the anesthetized marmoset. a) Two hybrid μECoG arrays placed over area V1 and MT in the marmoset visual cortex to guide the insertion of laminar arrays for paired multi-area laminar recordings in the primate visual hierarchy. **b)** μECoG electrodes demonstrated visual responsiveness and visual mapping could be performed to determine retinotopic organization across cortical areas. The retinotopic selectivity of neurons recorded from the depth matched well the selectivity expected based on surface recordings with the μEcoG as evident by the similarity of receptive fields from the depth probe and the neighboring μEcoG sites. **c)** Example single-trial LFP responses from a subset of simultaneously recorded μECoG channels. In the example trial shown, a full screen drifting grating was presented for a duration of 2 s. The onset and offset

314 of the visually evoked potentials are visible in the traces from area V1 and MT and **d)** across the depth of
315 the cortex simultaneously recorded from the laminar arrays in both areas. **e)** Example raster plots of spiking
316 activity recorded from the cortical depth with a laminar array in MT. Each block shows multiple trials of
317 visual stimulation with a particular stimulus orientation, demonstrating the ability of detailed functional
318 characterization of the neuronal populations underlying the µECoG.

319

320 **Hybrid µECoG for optogenetic mapping of local and inter-areal interactions**

321 We next took advantage of the optical access through the hybrid µECoG to perform local and
322 inter-areal optogenetic mapping. Prior to the recordings, cats and marmosets were injected with
323 adeno-associated viral (AAV) vectors to express channelrhodopsin in cortical pyramidal neurons
324 (CamKII promoter). After multiple weeks of expression, experiments were performed, in which we
325 positioned an optic fiber connected to a laser over the surface of the µECoG to permit direct
326 stimulation of neurons lying below. As previously mentioned, the µECoG permitted the localization
327 of populations expressing the transgene due to the attached fluorophore (Figure 2e). Visualization
328 and widefield fluorescence microscopy of the cortical surface through the µECoG enabled us to
329 directly target cortical populations expressing the excitatory opsin while avoiding large vasculature
330 (Figure 2e and Figure 5a).

331 In cat area 17, focal optogenetic activation of a local population of excitatory neurons expressing
332 an excitatory opsin (hChR2 under the CamKII promoter) increased neuronal activity detectable in
333 both MUA and gamma-band LFP power on the µEcoG array (Figure 5b and c). The topographical
334 pattern of this local activation could also be visualized across the cortical surface (Figure 5d and
335 e). Optogenetically activated neuronal activity in area 17 was localized to a focal area consistent
336 with the location of the laser, and increased MUA correlated with increased gamma-band power
337 as detected on the µECoG (Figure 5f). Similarly, in marmoset V1, optogenetic activation also led
338 to spatially localized MUA increase around the location of the laser (Figure 5g). The strong
339 feedforward projections from marmoset V1 to MT predict that activation of neurons in V1 lead to
340 spiking of neurons in MT. Indeed, we observed that stimulation with blue light stimulation in V1
341 caused short-latency responses in MT. There was no response to the yellow laser control
342 condition, indicating the responses were specific to activation of opsin expressing V1 neurons.

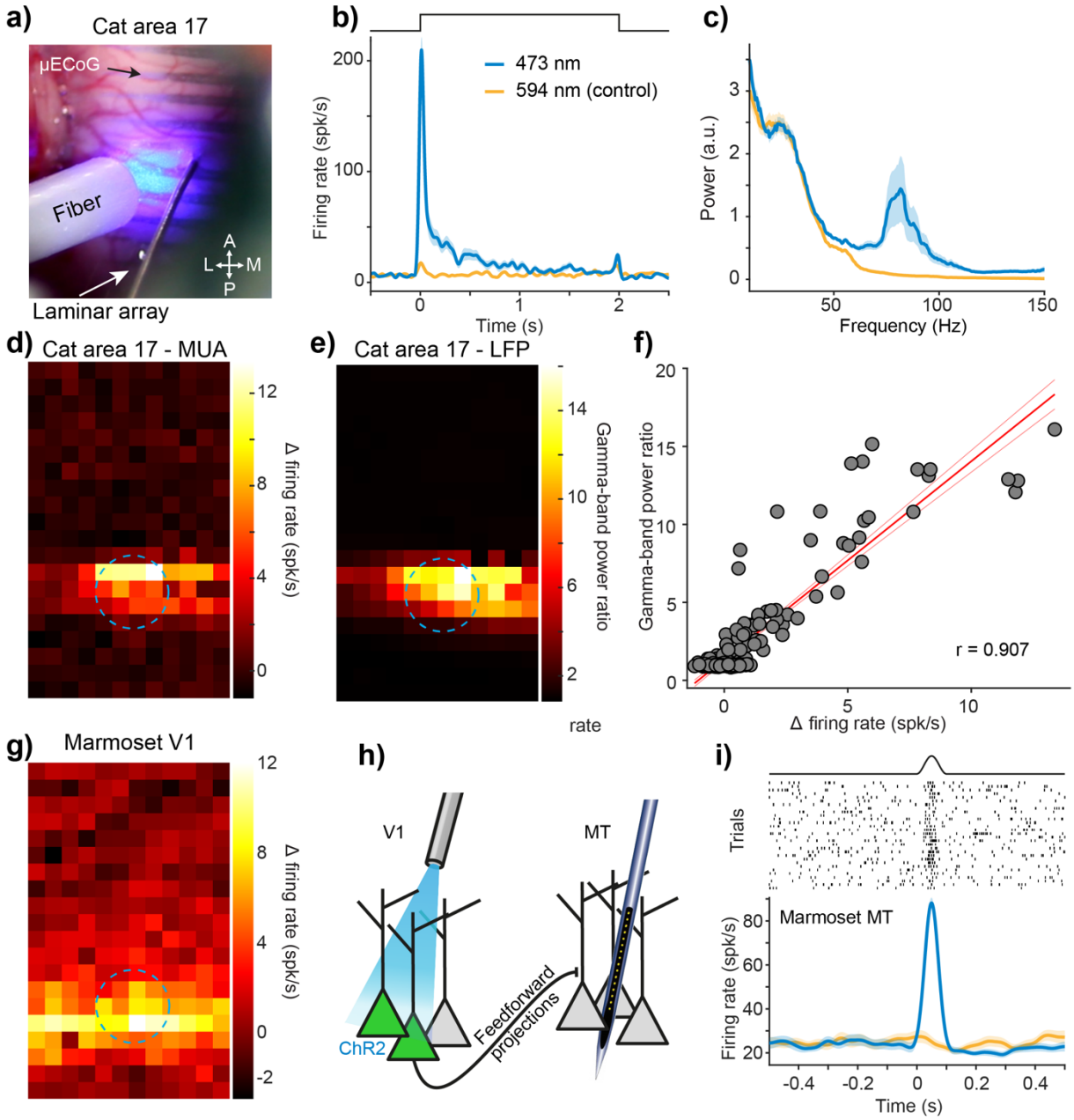

Figure 6: Hybrid μECoG permits local and interareal optogenetic mapping in the visual hierarchy. **a)** Photograph of a hybrid μECoG placed over area 17 of the anesthetized cat during simultaneous multi-area laminar recording and optogenetic stimulation of pyramidal neurons. **b)** A peristimulus time histogram of MUA activity recorded on the μECoG during optogenetic activation of neurons in area 17 (blue) or control (yellow). **c)** Power spectrum of LFP power recorded on the μECoG probe in area 17 to local optogenetic activation (blue) or control (yellow). **d)** Spatial response pattern of MUA activation over area 17 to focal optogenetic activation. **e)** Spatial response pattern of gamma-band power increase over area 17 to focal

352 optogenetic activation. Dashed blue circles in (d) and (e) indicate estimated laser location. **f)** Local
353 increases in MUA and gamma-band power correlate across the μECoG in area V1. **g)** Spatial response
354 pattern of MUA activation over marmoset V1 to focal optogenetic activation. **h)** Illustration of optogenetic
355 feed-forward neuronal activation of neurons projecting from area V1 to area MT as performed in our study.
356 **i)** MUA activity evoked in area MT to feedforward optogenetic activation of V1 neurons. MT laminar probe
357 was inserted based on functional mapping of area MT to retinotopically correspond to the V1 optogenetic
358 stimulation site.

359 **μECoG enables large-scale recording across the cat visual hierarchy**

360 Finally, we sought to perform large-scale recordings of activity across the visual hierarchy of the
361 cat using a combination of our hybrid μECoG and a commercially available μECoG developed
362 with an industry partner (CorTec GmbH, Freiburg, Germany). To this end, we worked with CorTec
363 GmbH to design and fabricate a lower-density pure PDMS μECoG array with 120 electrodes (0.2
364 mm diameter platinum-iridium electrode sites) arranged in a regular 6 x 20 electrode grid with 0.7
365 mm by 0.8 mm pitch (Figure S2a and b). The overall dimensions of the CorTec array were 4.5
366 mm by 16.2 mm, and it could be placed to cover multiple visual areas in the cat. Like our μECoG,
367 the CorTec μECoG was transparent (Figure 6a and b) and could be placed to cover multiple areas
368 in the cat visual cortex (Figure 6c). We placed the CorTec μECoG to cover the primary visual
369 cortex of the cat (areas 17 and 18) and performed functional mapping (retinotopy) of the
370 underlying cortex. LFP signals recorded from the CorTec μECoG could be used to determine the
371 visual selectivity of the underlying cortex, nicely demonstrating the difference in receptive field
372 size when moving from area 17 to area 18 (Figure 6d). Furthermore, as with our hybrid μECoG,
373 linear electrode arrays could be inserted to perform simultaneous functionally guided laminar
374 recordings (Figure 6b). We therefore attempted to scale up our μECoG-based recording of activity
375 across the visual hierarchy of the cat. Using 2 hybrid μECoG arrays and 5 silicone μECoG arrays,
376 we were able to cover large portions of the dorsal cortex of the cat bilaterally. We were able to
377 record simultaneous activity from 7 μECoG arrays totaling 1080 electrodes across 9 visual areas
378 bilaterally (Figure 6e). Example traces from the simultaneous μECoG recordings highlight the
379 possibility to investigate high-resolution signal flow across extended portions of the cortical
380 hierarchy (Figure 6f).

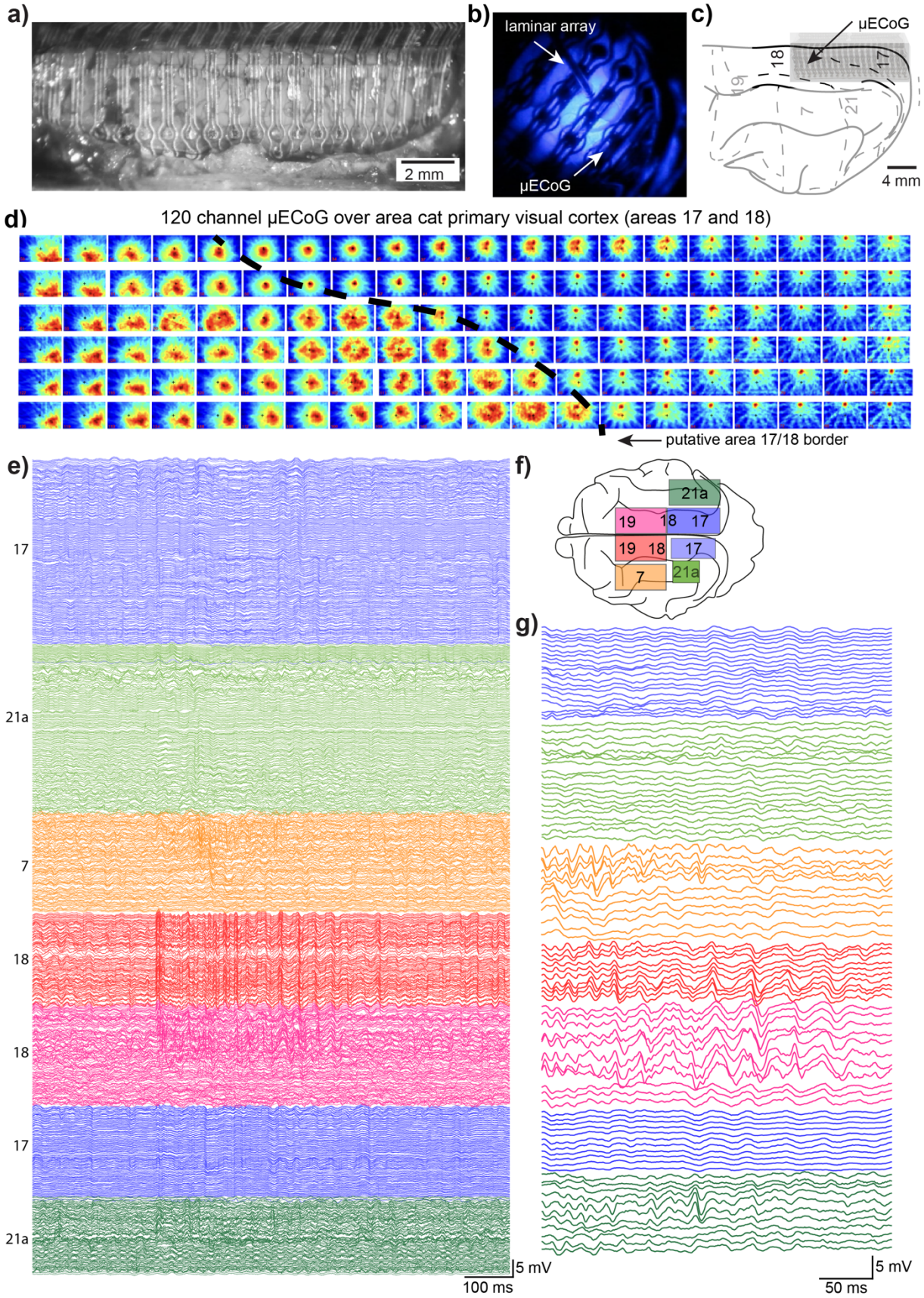
a)
2 mm
b)
laminar array
μECoG
c)
μECoG
18
17
19
7
21
4 mm
d)
120 channel μECoG over area cat primary visual cortex (areas 17 and 18)
putative area 17/18 border
e)
17
21a
7
18
18
17
21a
5 mV
100 ms
f)
21a
19
18
17
19
18
17
7
21a
g)
5 mV
50 ms

Figure 7: μECoG enables dense, multi-scale functional mapping of cortical activity across the visual system in the anesthetized cat. a) Photograph of a CorTeC μECoG in place over the cat primary visual cortex (areas 17 and 18). **b)** Photograph of blue excitation light from a laminar electrode array with integrated fiber-optics, transmitting through the cat visual cortex. **c)** Illustration of the μECoG array as targeted to the cat cortical atlas using anatomical coordinates to target primary visual cortex. **d)** Visual receptive fields recorded with the CorTec μECoG with the putative border between area 17 and 18 illustrated and visible in the larger sized receptive fields in area 18. **e)** 1080 channels of data recorded using two custom hybrid μECoG arrays and five commercial μECoG arrays across the visual system of the cat. **f)** Illustration of the placement of individual μECoG arrays over the dorsal cortex of the cat. **g)** Zoom-in on a selection of sites from each μECoG array showing fluctuations in the LFP recorded across visual areas.

Discussion

Brain activity displays exquisite coordination across spatial and temporal scales. New tools are required to simultaneously observe and manipulate multiscale brain activity, especially from anatomically connected populations distributed across brain-wide networks. We present a hybrid μECoG that enables functionally targeted multiscale investigations of local and distributed neural populations. We combined the advantages of two key, biocompatible flexible polymers to produce an ECoG array that had high electrode density, while conforming to soft neural tissue. By combining flexible, thin-film electrode arrays based on polyimide with a silicone elastomer substrate, we constructed a series of modular μECoG arrays that provided long-lasting, high-resolution recordings from distributed cortical brain areas. The two-step fabrication process isolated demanding clean-room fabrication from flexible, modular assembly of the final arrays to match different cortical areas of interest across the widely varying brain sizes of rats, cat and marmosets. We demonstrate functionally guided multi-area laminar recordings and inter-areal optogenetic activation to highlight the utility of this approach for investigating communication and coordination between distributed neuronal populations.

Our application of the hybrid μECoG demonstrates their utility for investigating the multi-scale and multi-area coordination of cortical signal flow. Despite reaching these goals, all our experiments were performed in anesthetized animals without the need to package the arrays in a robust fashion conducive to long-term chronic recording in awake, behaving animals. However, in principle these or similar arrays can be integrated with recording chambers and artificial dura replacement for chronic implantation in primates or cats[73–75], and related designs have been chronically implanted in mice for months.[50,76] Indeed, our use of silicone elastomers was inspired by their previous use as chronic dura-replacements to achieve long-term optical and electrical

access to the cortical surface.[58,65,66] Here we extend that use to enable functional mapping across multiple cortical areas, while permitting repeated targeted recording with penetrating electrodes and laminar arrays. Our design enabled simultaneous recording from neuronal populations in the depth due to the soft PDMS encapsulation that could be penetrated with stiff, linear electrode arrays, resealing after penetration. Furthermore, our design provided relatively unobscured optical access to the underlying tissue. The hybrid μECoG array was also robust and we were able to use them repeatedly in multiple experiments spanning years, if it was cleaned and safely stored between uses. The optical transparency of PDMS also permits combined optical recordings with the presented design, which can facilitate further elucidation of the cellular and subcellular processes involved in local and interareal interactions.[16,50]

In principle, inter-areal investigations can also be performed in an all-optical fashion by co-expressing genetically encoded activity indicators and excitatory or inhibitory opsins in cells of interest. While such methods have been impressively demonstrated in the mouse[77–80], they have not yet been achieved in the larger brains of the cat or primate. Although 2-photon imaging has been increasingly used in primates,[81–83] the transfer of appropriate viruses and molecular tools, as well as suitable optical systems to the considerably larger feline or primate brain is non-trivial. Considerable difficulties may arise due to challenges with viral co-infection, larger distances between relevant areas and increased brain movement in larger animals. That being said, optical methods can enable higher specificity by enabling viral and genetic approaches to target specific populations and project pathways. However, even the most advanced optical methods, using genetically encoded voltage indicators cannot detect single spikes with millisecond precision across populations that span several millimeters.[84] Therefore, we believe that the combined use of optical and electrical recording methods provides the opportunity for synergistic, multimodal investigations of brain function.[16,50] Future work could establish such hybrid μECoG arrays as a platform for chronic brain interfaces to enable long-term multi-scale optical and electrophysiological recording of brain activity.

While functional mapping with μECoG and subsequent local recording with multi-electrode arrays can be performed sequentially, the combined application of large-scale and dense measurement methodologies simultaneously permits local cellular activity to be evaluated in the context of ongoing patterns of brain wide activity with which it is coordinated.[15,16,25] Such investigations have begun to reveal the importance of multi-scale studies for interpreting the responses of single cells in the context of local circuit activity and situating local patterns in global brain states.[9,25,30,31,85,86] Functional mapping also permits targeted injection of viruses or pharmacological agents, further

expanding the possibilities of combined μECoG and depth electrode or optical studies. For example, viral transfection of opto- or chemogenetic effectors into local or long-range projections can permit functionally characterized populations to be activated or silenced, expanding the possibilities to dissect inter-areal interactions[87,88]. Likewise, viral transfection of genetically encoded activity indicators can permit simultaneous optical recording of cellular signals in the local population or identified projections, such as long-range neuronal or neuromodulatory projections that might affect local or inter-areal dynamics.[30,89–92] The combination of electrical recording with optical methods, such as imaging,[16,85,93] or optical perturbations[27,87,94,95] can permit fined-grained investigations that further reveal the cellular processes underlying coordinated dynamics and inter-areal interactions. New techniques and tools to measure and manipulate brain activity have revolutionized our understanding of healthy and disordered brain function. The hybrid μECoG we developed enables the combination of simultaneous optical and electrophysiological measurement from functionally characterized local and distributed neuronal populations. Such tools and the studies they enable will allow refined investigation of inter-areal information transfer and the local and distributed processes underlying adaptive behavior.

Methods

ECoG fabrication

The hybrid µECoG arrays were fabricated in a two-stage process. First, flexible, linear arrays were fabricated using photolithography to structure platinum on polyimide thin films. Second, these arrays were arranged in a regular pattern and bonded to a PDMS superstructure.

Fabrication of flexible linear arrays. Using standard MEMS cleanroom techniques as previously published,[47,62,64] we fabricated 12 or 24 contact linear arrays on polyimide with 35 µm diameter platinum contacts. Briefly, we spin-coated a 5 µm layer of polyimide (U-Varnish S, UBE) on a silicon wafer and imidized it in a vacuum oven at 450 °C. Next, activation was performed with O_2-plasma (30 s, 100 W), and we sputtered a 300 nm layer of platinum onto the polyimide and defined electrodes and tracks with photolithography. The metal tracks were insulated with a second layer of polyimide (5 µm). Finally, the electrode pads and the overall linear array shape were defined via reactive ion etching in an O_2-plasma.

Integration with PDMS. The previously fabricated linear arrays were arranged into the desired pattern and then integrated to the PDMS superstructure. First, we arranged the linear arrays into a regular 2D sheet by placing them with the exposed electrode surface facing down onto a clean glass slide that was placed over millimeter grid-paper. Under stereoscope guidance and with the aid of the grid-paper, we aligned the polyimide linear arrays by hand to the desired spacing and coverage. To prevent accidental misalignment of the arrays or unintended occlusion of electrode contacts, we did not pour fluid PDMS on top of the polyimide strips for in-situ polymerization. Rather, a previously polymerized PDMS sheet (0.5-0.8mm thickness) was cut to the desired size and then placed on top of the polyimide arrays. Next, any misalignment was manually corrected, and PDMS was applied to the front and the back of the arrays. This prevented any leakage of liquid PDMS onto the electrode contacts, which could lead to impedance increase or full electrical insulation, thereby rendering them non-functional. Lastly, the metal wire holders were lowered onto the assembly with a manual micromanipulator and more PDMS was applied to attach the holders to the PDMS sheet. We used a two-component PDMS (Biopor AB, 25 Shore) for all manufacturing steps. PDMS curing was performed at room temperature.

Animals

Two adult male Sprague-Dawley rats (Rattus norvegicus), three adult domestic cats (*Felis catus*; 2 females), and two adult male marmosets (Callithrix jacchus) were used in this study. We used multiple organisms to establish the utility of the approach across diverse model species. All procedures complied with the German law for the protection of animals and were approved by the regional authority (Regierungspräsidium Darmstadt). After an initial surgery for the injection of viral vectors and a 4-6 week period for opsin expression, recordings were obtained during a terminal experiment under general anesthesia.

500 **Viral vector injection**

501 ***Cats.*** Anesthesia was induced by intramuscular (i.m.) injection of ketamine (10 mg/kg) and
502 dexmedetomidine (0.02 mg/kg). Cats were intubated and anesthesia was maintained with N_2O:O_2
503 (60/40%), isoflurane (~1.5-2.5%) and remifentanil (0.3 µg/kg/min). Rectangular craniotomies
504 were performed with an ultrasonic bone drill (Piezosurgery, Mectron) over area 17 and the dura
505 mater was removed. The target location in area 17 was guided by stereotaxic coordinates[96] and
506 by the local pattern of sulci and gyri. Three to four injection sites were chosen, avoiding blood
507 vessels, with horizontal distances between injection sites of at least 1 mm. At each site, a Hamilton
508 syringe (34G or 35G needle size; NanoFil syringe, World Precision Instruments) was inserted with
509 the use of a micromanipulator (David Kopf Instruments) and under visual inspection to a cortical
510 depth of 1 mm below the pia mater (0.5mm below pia in the rat). Subsequently, 2 µl of viral vector
511 dispersion was injected at a rate of 150 nl/min with a microinjector pump (UMP3-1, World
512 Precision Instruments). After each injection, the needle was left in place for 10 min before
513 withdrawal, to avoid reflux. Upon completion of injections, the dura opening was covered with
514 silicone foil and a thin layer of silicone gel, the trepanation was filled with dental acrylic, and the
515 scalp was sutured.

516 In all cats, area 17 of the left hemisphere was injected with AAV1-CamKIIα-hChR2(H134R)-eYFP
517 (titer: $1.22*10^{13}$ GC/ml).

518 ***Marmosets.*** Anesthesia was induced via i.m. injection of alfaxalone (8.75 mg/kg) and diazepam
519 (0.625 mg/kg), then maintained with isoflurane (~1.5–2.5%) delivered through a nose cone in one
520 animal and through an endotracheal tube in the other animal. Buprenorphine (0.05 mg/kg) was
521 administered pre-surgery for analgesia. A small burr hole (~3 mm) was drilled over the target site
522 in the left primary visual cortex guided by stereotaxic coordinates[97] and the dura was carefully
523 incised using the bent tip of a hypodermic needle. A Hamilton syringe with a 35G needle (NanoFil
524 syringe, World Precision Instruments), mounted on a micromanipulator (David Kopf Instruments)
525 was then slowly lowered into the brain. One animal received injections at two sites within the
526 same craniotomy at depths of 0.8 mm and 0.5 mm, with 2 µL delivered per site. The other animal
527 was injected at a single site with 1.6 µL. In both animals, AAV1-CamKIIα-hChR2(H134R)-eYFP
528 viral vectors were injected at 200 nL/min. After injection, the trepanation was covered with dental
529 acrylic, and the scalp was sutured.

530 ***Rats.*** Anesthesia was induced by i.m. injection of ketamine (100 mg/kg) and dexmedetomidine
531 (0.25 mg/kg), then maintained with isoflurane (~1.5–2.5%) in 100% oxygen delivered through a
532 nose cone. The viral vector injection was performed in the primary visual cortex[98] and the
533 procedure was otherwise identical to that described for the marmoset.

534

535 All injections were performed under aseptic conditions for rats and under sterile conditions for
536 marmosets and cats. The DNA plasmids were provided by Dr. Karl Deisseroth (Stanford
537 University, Stanford, CA). AAV1 and AAV9 viral vectors were obtained from Penn Vector Core
538 (Perelman School of Medicine, University of Pennsylvania, USA).

539 **Neurophysiological recordings - cat**

540 For recording experiments, anesthesia was induced and initially maintained as during the injection
541 surgery, only replacing intubation with tracheotomy and remifentanyl with sufentanil. After
542 surgery, during recordings, isoflurane concentration was lowered to 0.6%-1.0%, eye lid closure
543 reflex was tested to verify narcosis, and vecuronium (0.25mg/kg/h i.v.) was added for paralysis
544 during recordings to prevent reflexive eye movements. Throughout surgery and recordings,
545 Ringer solution plus 10% glucose was given (20 ml/h during surgery; 7 ml/h during recordings),
546 and vital parameters such as ECG, body temperature and end-tidal CO_2 were monitored
547 continuously.

548 **Neurophysiological recordings - marmoset**

549 For recording experiments, anesthesia was induced and initially maintained as during the injection
550 surgery. A tracheotomy was performed and sufentanil (4-8 µg/kg/h) was continuously infused
551 intravenously in Ringer solution containing 5% amino acids and 3% glucose. After surgery, during
552 recordings, isoflurane concentration was lowered to 0.5%-1.5%, eye lid closure reflex was tested
553 to verify narcosis, and vecuronium (0.2 mg/kg/h) was added for paralysis during recordings to
554 prevent reflexive eye movements. Throughout surgery and recordings, vital parameters such as
555 ECG, body temperature and end-tidal CO_2 were monitored continuously.

556 **Neurophysiological recordings - rat**

557 For recording experiments, anesthesia was induced and maintained as during the injection
558 surgery.

559 **Neurophysiological recordings - general**

560 Each experiment consisted of multiple recording blocks of data acquisition per animal. Large
561 rectangular craniotomies were made and the dura was removed to permit placement of µECoG
562 arrays directly on the brain surface in the respective areas. For depth recordings, several
563 electrode types were inserted though the µECoG: Tungsten microelectrodes (~1 MΩ impedance
564 at 1 kHz; FHC), 32- or 128-contact silicon probes (50 or 100 µm inter-contact spacing;
565 NeuroNexus or ATLAS Neuroengineering), and 16- or 24-contact linear electrode arrays (V- and
566 U-probes; Plexon). In one cat, one 16-contact probe with 150 µm inter-contact spacing and one
567 46 µm optic fiber, and one 16-contact probe with 150 µm inter-contact spacing and four 46 µm
568 optic fibers were used (Plexon V- and U-probe, respectively). Neural signals were recorded with
569 the OpenEx suite software package (Tucker Davis Technologies) through active, unity gain head

570 stages (ZC32, ZC64 and ZC128, Tucker Davis Technologies) and digitized at 24,414.0625 Hz
571 (PZ2 preamplifier, Tucker Davis Technologies). For MUA recordings, the signals were filtered with
572 a passband of 700 to 7000 Hz, and thresholds were set to retain the spike times of small clusters
573 of units. For LFP recordings, the signals were filtered with a passband of 0.7 to 250 Hz, digitized
574 at 1017.1 Hz and resampled to 1 kHz for analysis.

575 **Visual stimulation**

576 Visual stimuli were displayed on a gamma-corrected TFT monitor (Samsung SyncMaster
577 2233RZ) at a refresh rate of 120 Hz and generated via custom MATLAB (MathWorks) code and
578 Psychtoolbox-3.[99] In cats and marmosets, contact lenses were used to prevent drying of the
579 cornea and to assure correct focus of the visual stimuli onto the retina.

580 **Optogenetic stimulation**

581 Optogenetic stimulation was performed with a 473 nm (blue) laser or with a 470 nm (blue) LED
582 (Omicron Laserage). A 594 nm (yellow) laser was used as randomly interleaved control. Laser
583 light was delivered to the cortical surface through a 100 µm or a 200 µm diameter multimode fiber
584 (Thorlabs), LED light through a 2 mm diameter polymer optical fiber (Omicron Laserage). Fiber
585 endings were placed just above the cortical surface, immediately next to the recording sites with
586 a slight angle relative to the electrodes. Laser waveform generation used custom circuits in TDT,
587 and timing control used Psychtoolbox-3, a toolbox in MATLAB.

588 **Data analysis**

589 All data analysis was performed using custom code and the Fieldtrip toolbox (Oostenveld et al.,
590 2011), both written in MATLAB (MathWorks). PSTH plots for MUA rates were smoothed with a
591 Gaussian window (SD = 10 ms). For receptive field mapping analysis from LFPs, signals were
592 band-pass filtered with a Butterworth filter between 60 and 90Hz (filter order = 2). The absolute
593 amplitude of the Hilbert transform of this signal was then used to generate a trial averaged,
594 smoothed PSTH (SD = 60 ms) for each of the 16 directions of the moving bar. The value at a
595 delay of 50 ms was used as the magnitude of visual response at the corresponding location in
596 visual space and the 2D receptive field image was spatially smoothed (SD = 25.5 pixels).
597 Receptive field mapping analysis from MUA data was identical, except that the PSTH was
598 calculated from smoothed spiking data (SD = 60 ms).

599 The center of each receptive field was calculated by thresholding the normalized 2D receptive
600 field image data at a value of 0.7 and then calculating the center of mass. Retinotopic maps for
601 the full areas covered by the µECoGs where then generated from the resulting receptive field
602 centers. The map was upscaled by a factor of 50 using bicubic interpolation and smoothed with
603 a Gaussian filter (SD = 50 pixels). For the maps from cat area 21a (Figure 3h), 8 out of 240
604 channels were excluded and interpolated because they appeared electrically shortened, as

indicated by an abnormally high correlation with other channels (defined as a Pearson correlation >0.97 with at least 8 other channels). For the correlation of LFP-based with spike-based receptive field coordinates, we only included channels with a signal-to-noise ratio (SNR) > 2.5. SNR was defined as the ratio of the pixel values inside the normalized receptive field (all pixels that were >0.7) and the rest of the image, resulting in 138 out of 240 channels being included in the analysis (Figure 3g).

LFP time-frequency analysis was calculated for data epochs that were adjusted for each frequency to have a length of 4 cycles and moved over the data in a sliding-window fashion in 1-ms steps. Each epoch was multiplied with a Hann taper, Fourier transformed, squared and divided by the window length to obtain power density per frequency. For the different stimulation frequencies f, LFP power is shown as percent change of power during stimulation versus pre-stimulation baseline.

For 2D correlation analysis between ECoG and laminar probe signals, data was band pass filtered with a second order Butterworth filter (10-20 Hz or 100-200 Hz), z-scored and corrected for median channel activity per channel. The first second of the data after stimulus onset from all 8 stimulus orientation conditions was used to calculate the Pearson correlation coefficients for all ECoG channels against individual laminar probe channels.

Acknowledgements

We thank Thomas Wunderle and Gustavo Rohenkohl for their assistance during a portion of the experiments. This work was supported by DFG (SPP 1665 FR2557/1-1, FOR 1847 FR2557/2-1, FR2557/5-1-CORNET, FR2557/6-1-NeuroTMR, FR2557/7-1-DualStreams to P.F.), EU (HEALTH-F2-2008-200728-BrainSynch, FP7-604102-HBP, FP7-600730-Magnetrodes to P.F.), National Institutes of Health (1U54MH091657-WU-Minn-Consortium-HCP to P.F.), the LOEWE program (NeFF to P.F.) and the University of Zurich (project K-41220-04, C.L.).

Author contributions

P.J, P.F., and C.M.L. designed research; B.R., R.L. and T.S. fabricated the polyimide electrode arrays, P.J. and C.M.L. performed experiments; P.J. and C.M.L. analyzed data; P.F. and C.M.L. provided supervision, C.M.L. and P.J. wrote the paper with input from the other authors.

Declaration of Interests

P.F. and C.M.L. have a patent on insertion methods for thin-film electrodes. P.F. is member of the Advisory Board of CorTec GmbH (Freiburg, Germany). T.S. is one of the co-founders and member of the Scientific Technical Advisory Board of CorTec GmbH (Freiburg, Germany).

Supplementary Figures

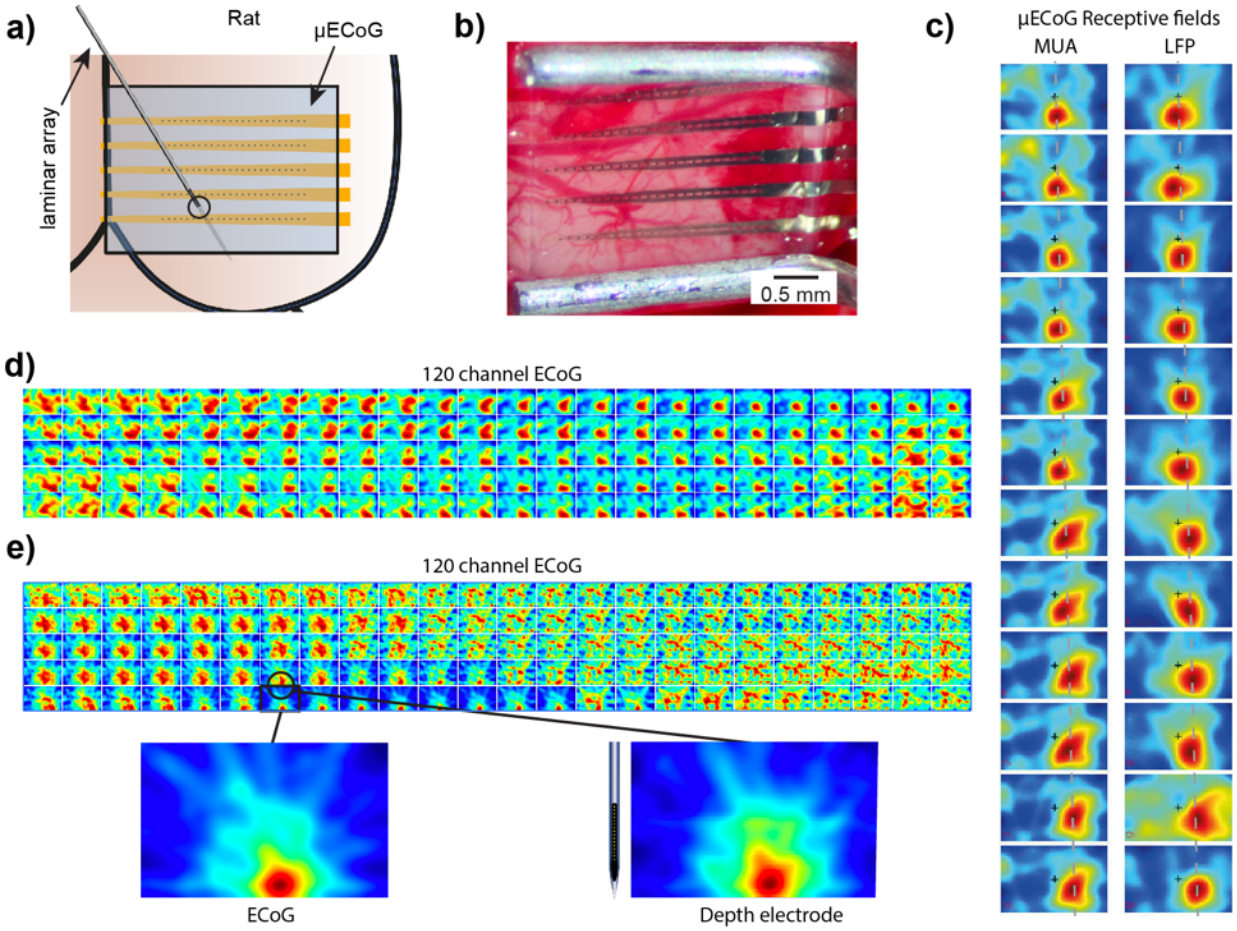

Supplementary Figure 1 Hybrid μECoG functional mapping of rodent visual cortex (A) Illustration of the hybrid μECoG placed over the posterior dorsal cortex of the rat brain with a laminar array penetrating the μECoG into the cortical depth. b) Photograph of a hybrid μECoG in position above the rat posterior cortex. c) Comparison of RF estimates from MUA or LFP (power in the 60-100 Hz band) recorded from a μECoG array placed above the rat visual cortex. d) Example visual RF estimates across the rat visual cortex using a hybrid μECoG. e) Example of visual receptive fields estimated from μECoG recordings (left bottom panel) and from a laminar electrode array inserted through the μECoG to the cortical depth (right bottom panel).

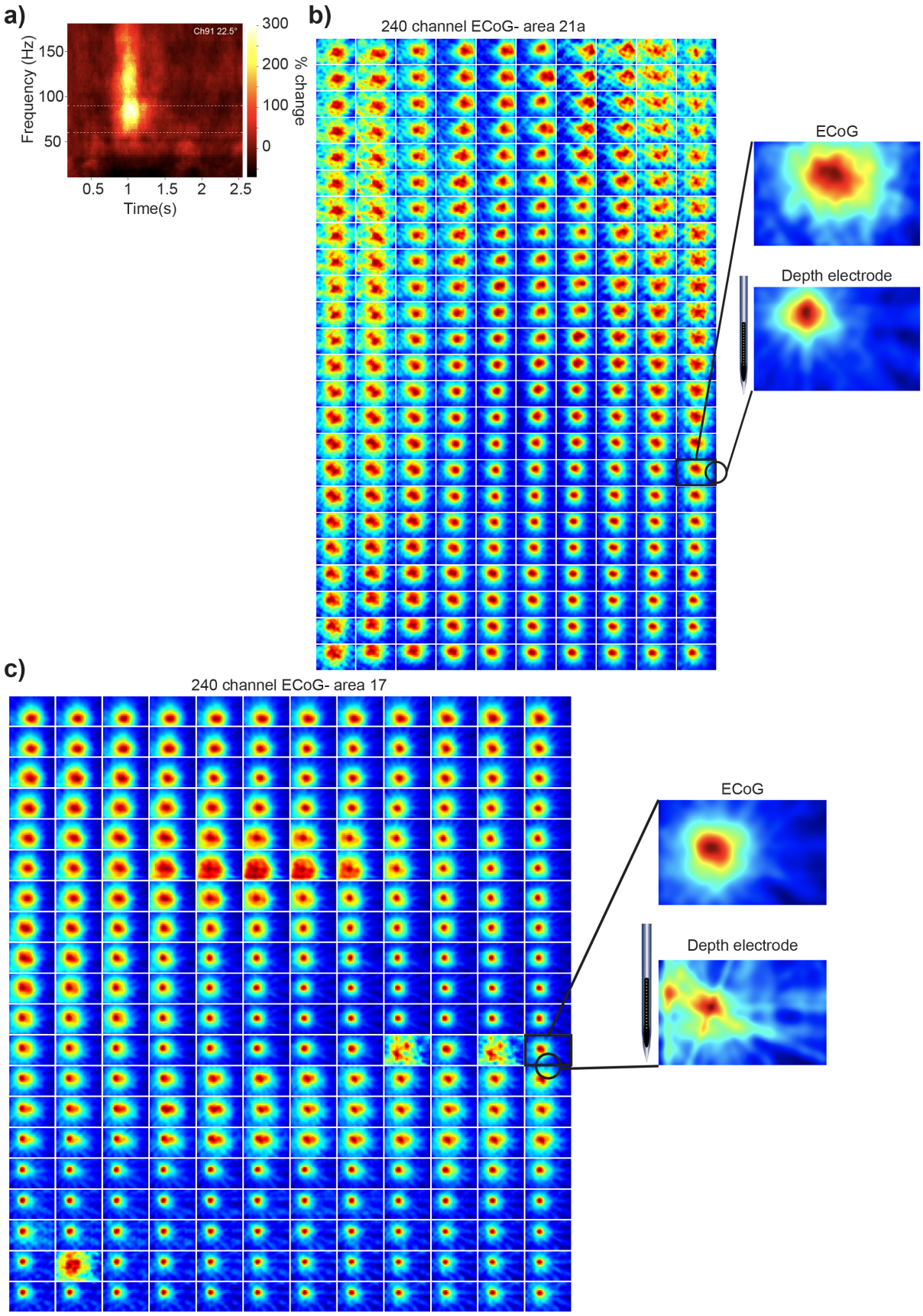
a)
Ch91 22.5°
Frequency (Hz)
150
100
50
0.5
1
1.5
2
2.5
Time(s)
300
200
100
0
% change
b)
240 channel ECoG- area 21a
ECoG
Depth electrode
c)
240 channel ECoG- area 17
ECoG
Depth electrode

648

Supplementary Figure 2 Receptive fields estimated from µECoG in areas 17/18 and 21a of the cat visual cortex. a) Example time-frequency plot of the LFP response to visual stimulation with the RF mapping protocol. A transient increase in power in the frequencies above 60 Hz is visible. For the LFP RF mapping, we used the gamma-band power to estimate the RF for each µECoG electrode. **b)** The RF for each µECoG electrode for the array placed over area 17/18 are plotted as a function of position on the ECoG array. (right) The RFs estimated using LFP from the ECoG agree well with RFs estimated from neuronal MUA activity recorded in the depth using linear electrode arrays. **c)** RFs mapped from LFP power for the ECoG in area 21a. Subplots on the right show a magnified view of the RFs from the depth electrode (bottom), inserted into the cortex through the ECoG and the receptive field of the immediately neighboring EGoG electrode (top), revealing very similar spatial selectivity. Note that the RF maps for the area 17 and 21a ECoG arrays are drawn in scale in coordinates of the visual display and do not reflect the relative physical dimensions of the ECoG arrays.

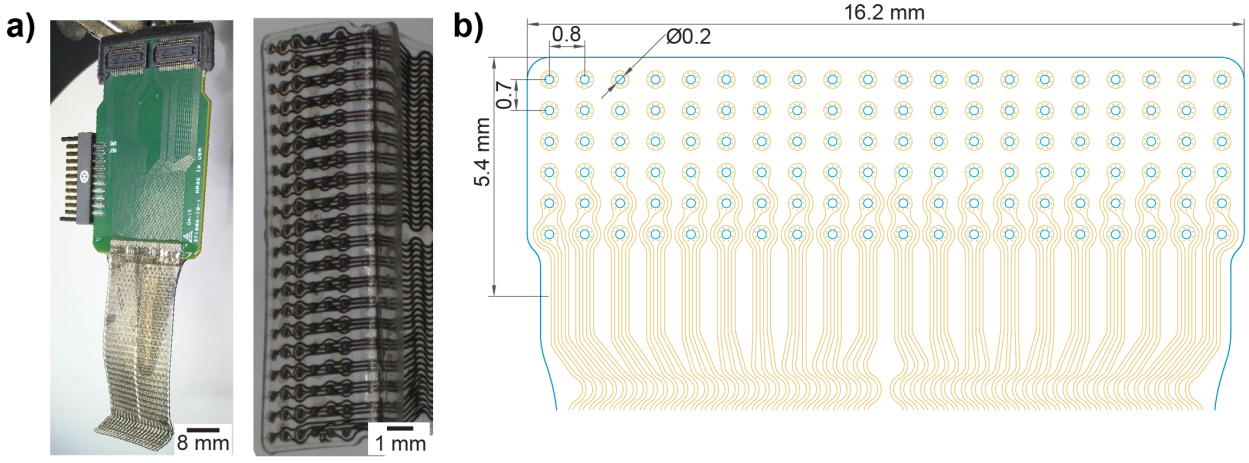

Supplementary Figure 3 Silicone µECoG fabricated by CorTec GmbH. a) Left, Photograph of assembled µECoG and connector board. Right, Zoomed photograph showing the µECoG array electrodes and traces. Compared to our hybrid µECoG, more of the field of view is obscured by electrodes and wiring, because of the lower resolution of the pure PDMS µECoG. b) Schematic layout of the CorTec PDMS µECoG design.

671 **References**

[1] W. E. Allen, M. Z. Chen, N. Pichamoorthy, R. H. Tien, M. Pachitariu, L. Luo, K. Deisseroth, *Science* **2019**, *364*, eaav3932.
[2] N. A. Steinmetz, P. Zatka-Haas, M. Carandini, K. D. Harris, *Nature* **2019**, *576*, 266.
[3] P. R. Roelfsema, A. K. Engel, P. König, W. Singer, *Nature* **1997**, *385*, 157.
[4] M. A. L. Nicolelis, A. A. Ghazanfar, B. M. Faggin, S. Votaw, L. M. O. Oliveira, *Neuron* **1997**, *18*, 529.
[5] K. L. Hoffman, B. L. McNaughton, *Science* **2002**, *297*, 2070.
[6] E. M. R. Lake, X. Ge, X. Shen, P. Herman, F. Hyder, J. A. Cardin, M. J. Higley, D. Scheinost, X. Papademetris, M. C. Crair, R. T. Constable, *Nat Methods* **2020**, *17*, 1262.
[7] J. A. Cardin, M. C. Crair, M. J. Higley, *Neuron* **2020**, *108*, 33.
[8] D. Barson, A. S. Hamodi, X. Shen, G. Lur, R. T. Constable, J. A. Cardin, M. C. Crair, M. J. Higley, *Nat Methods* **2020**, *17*, 107.
[9] N. K. Logothetis, O. Eschenko, Y. Murayama, M. Augath, T. Steudel, H. C. Evrard, M. Besserve, A. Oeltermann, *Nature* **2012**, *491*, 547.
[10] A. Sirota, J. Csicsvari, D. Buhl, G. Buzsáki, *Proc. Natl. Acad. Sci. U.S.A.* **2003**, *100*, 2065.
[11] H. B. Barlow, *Perception* **1972**, *1*, 371.
[12] A. J. Parker, W. T. Newsome, *Annu. Rev. Neurosci.* **1998**, *21*, 227.
[13] M. Mishkin, L. G. Ungerleider, K. A. Macko, *Trends in Neurosciences* **1983**, *6*, 414.
[14] R. E. Passingham, K. E. Stephan, R. Kötter, *Nat Rev Neurosci* **2002**, *3*, 606.
[15] T. A. Machado, I. V. Kauvar, K. Deisseroth, *Nat Rev Neurosci* **2022**, *23*, 683.
[16] C. M. Lewis, A. Hoffmann, F. Helmchen, *Neurophoton.* **2024**, *11*.
[17] S. L. Bressler, V. Menon, *Trends in Cognitive Sciences* **2010**, *14*, 277.
[18] R. Yuste, *Nat Rev Neurosci* **2015**, *16*, 487.
[19] F. Varela, J.-P. Lachaux, E. Rodriguez, J. Martinerie, *Nat Rev Neurosci* **2001**, *2*, 229.
[20] C. Koch, *Biophysics of computation: information processing in single neurons*, Oxford University Press, New York **2020**.
[21] D. Beniaguev, I. Segev, M. London, *Neuron* **2021**, *109*, 2727.
[22] C. Koch, I. Segev, *Nat Neurosci* **2000**, *3*, 1171.
[23] R. B. Ebitz, B. Y. Hayden, *Neuron* **2021**, *109*, 3055.
[24] G. Buzsáki, *Nat Neurosci* **2004**, *7*, 446.
[25] T. A. Engel, M. L. Schölvinck, C. M. Lewis, *NeuroImage* **2021**, *245*, 118692.
[26] M. Shein-Idelson, L. Pammer, M. Hemberger, G. Laurent, *Nat Methods* **2017**, *14*, 882.
[27] T. Marques, J. Nguyen, G. Fioreze, L. Petreanu, *Nat Neurosci* **2018**, *21*, 757.
[28] X. Jia, S. Tanabe, A. Kohn, *Neuron* **2013**, *77*, 762.
[29] J. D. Semedo, A. I. Jasper, A. Zandvakili, A. Krishna, A. Aschner, C. K. Machens, A. Kohn, B. M. Yu, *Nat Commun* **2022**, *13*, 1099.
[30] J. M. Shine, E. J. Müller, B. Munn, J. Cabral, R. J. Moran, M. Breakspear, *Nat Neurosci* **2021**, *24*, 765.
[31] B. R. Munn, E. J. Müller, I. Favre-Bulle, E. Scott, J. T. Lizier, M. Breakspear, J. M. Shine, *Cell* **2024**, S0092867424011528.
[32] C. Grienberger, A. Giovannucci, W. Zeiger, C. Portera-Cailliau, *Nature Reviews Methods Primers* **2022**, *2*, 67.
[33] F. Helmchen, W. Denk, *Nat Methods* **2005**, *2*, 932.
[34] M. Z. Lin, M. J. Schnitzer, *Nat Neurosci* **2016**, *19*, 1142.
[35] L. Luo, E. M. Callaway, K. Svoboda, *Neuron* **2008**, *57*, 634.
[36] A. R. Nectow, E. J. Nestler, *Nat Rev Neurosci* **2020**, *21*, 669.
[37] J. L. Chen, S. Carta, J. Soldado-Magraner, B. L. Schneider, F. Helmchen, *Nature* **2013**, *499*, 336.

[38] J. L. Chen, D. J. Margolis, A. Stankov, L. T. Sumanovski, B. L. Schneider, F. Helmchen, *Nat Neurosci* **2015**, *18*, 1101.
[39] M. M. Roth, J. C. Dahmen, D. R. Muir, F. Imhof, F. J. Martini, S. B. Hofer, *Nat Neurosci* **2016**, *19*, 299.
[40] N. J. Sofroniew, J. D. Cohen, A. K. Lee, K. Svoboda, *J. Neurosci.* **2014**, *34*, 9537.
[41] C.-H. Yu, J. N. Stirman, Y. Yu, R. Hira, S. L. Smith, *Nat Commun* **2021**, *12*, 6639.
[42] J. L. Chen, F. F. Voigt, M. Javadzadeh, R. Krueppel, F. Helmchen, *eLife* **2016**, *5*, e14679.
[43] G. N. Angotzi, F. Boi, A. Lecomte, E. Miele, M. Malerba, S. Zucca, A. Casile, L. Berdondini, *Biosensors and Bioelectronics* **2019**, *126*, 355.
[44] J. J. Jun, N. A. Steinmetz, J. H. Siegle, D. J. Denman, M. Bauza, B. Barbarits, A. K. Lee, C. A. Anastassiou, A. Andrei, Ç. Aydın, M. Barbic, T. J. Blanche, V. Bonin, J. Couto, B. Dutta, S. L. Gratiy, D. A. Gutnisky, M. Häusser, B. Karsh, P. Ledochowitsch, C. M. Lopez, C. Mitelut, S. Musa, M. Okun, M. Pachitariu, J. Putzeys, P. D. Rich, C. Rossant, W. Sun, K. Svoboda, M. Carandini, K. D. Harris, C. Koch, J. O'Keefe, T. D. Harris, *Nature* **2017**, *551*, 232.
[45] M. Siegel, T. J. Buschman, E. K. Miller, *Science* **2015**, *348*, 1352.
[46] J. H. Siegle, X. Jia, S. Durand, S. Gale, C. Bennett, N. Graddis, G. Heller, T. K. Ramirez, H. Choi, J. A. Luviano, P. A. Groblewski, R. Ahmed, A. Arkhipov, A. Bernard, Y. N. Billeh, D. Brown, M. A. Buice, N. Cain, S. Caldejon, L. Casal, A. Cho, M. Chvilicek, T. C. Cox, K. Dai, D. J. Denman, S. E. J. De Vries, R. Dietzman, L. Esposito, C. Farrell, D. Feng, J. Galbraith, M. Garrett, E. C. Gelfand, N. Hancock, J. A. Harris, R. Howard, B. Hu, R. Hytnen, R. Iyer, E. Jessett, K. Johnson, I. Kato, J. Kiggins, S. Lambert, J. Lecoq, P. Ledochowitsch, J. H. Lee, A. Leon, Y. Li, E. Liang, F. Long, K. Mace, J. Melchior, D. Millman, T. Mollenkopf, C. Nayan, L. Ng, K. Ngo, T. Nguyen, P. R. Nicovich, K. North, G. K. Ocker, D. Ollerenshaw, M. Oliver, M. Pachitariu, J. Perkins, M. Reding, D. Reid, M. Robertson, K. Ronellenfitch, S. Seid, C. Slaughterbeck, M. Stoecklin, D. Sullivan, B. Sutton, J. Swapp, C. Thompson, K. Turner, W. Wakeman, J. D. Whitesell, D. Williams, A. Williford, R. Young, H. Zeng, S. Naylor, J. W. Phillips, R. C. Reid, S. Mihalas, S. R. Olsen, C. Koch, *Nature* **2021**, *592*, 86.
[47] B. Rubehn, C. Bosman, R. Oostenveld, P. Fries, T. Stieglitz, *J. Neural Eng.* **2009**, *6*, 036003.
[48] J. Viventi, D.-H. Kim, L. Vigeland, E. S. Frechette, J. A. Blanco, Y.-S. Kim, A. E. Avrin, V. R. Tiruvadi, S.-W. Hwang, A. C. Vanleer, D. F. Wulsin, K. Davis, C. E. Gelber, L. Palmer, J. Van Der Spiegel, J. Wu, J. Xiao, Y. Huang, D. Contreras, J. A. Rogers, B. Litt, *Nat Neurosci* **2011**, *14*, 1599.
[49] D. Khodagholy, J. N. Gelinas, T. Thesen, W. Doyle, O. Devinsky, G. G. Malliaras, G. Buzsáki, *Nat Neurosci* **2015**, *18*, 310.
[50] A. F. Renz, J. Lee, K. Tybrandt, M. Brzezinski, D. A. Lorenzo, M. Cerra Cheraka, J. Lee, F. Helmchen, J. Vörös, C. M. Lewis, *Adv Healthcare Materials* **2020**, *9*, 2000814.
[51] C. Lewis, C. Bosman, P. Fries, *Current Opinion in Neurobiology* **2015**, *32*, 68.
[52] H. Ko, S. B. Hofer, B. Pichler, K. A. Buchanan, P. J. Sjöström, T. D. Mrsic-Flogel, *Nature* **2011**, *473*, 87.
[53] K. D. Harris, T. D. Mrsic-Flogel, *Nature* **2013**, *503*, 51.
[54] C. M. Lewis, C. A. Bosman, T. Womelsdorf, P. Fries, *Proc. Natl. Acad. Sci. U.S.A.* **2016**, *113*.
[55] M. Fukushima, R. C. Saunders, D. A. Leopold, M. Mishkin, B. B. Averbeck, *Neuron* **2012**, *74*, 899.
[56] V. B. Mountcastle, *Journal of Neurophysiology* **1957**, *20*, 408.
[57] Z. Wang, L. M. Chen, L. Négyessy, R. M. Friedman, A. Mishra, J. C. Gore, A. W. Roe, *Neuron* **2013**, *78*, 1116.
[58] C. Heo, H. Park, Y.-T. Kim, E. Baeg, Y. H. Kim, S.-G. Kim, M. Suh, *Sci Rep* **2016**, *6*, 27818.
[59] A. Arieli, A. Grinvald, *Journal of Neuroscience Methods* **2002**, *116*, 15.
[60] M. Vomero, M. F. Porto Cruz, E. Zucchini, F. Ciarpella, E. Delfino, S. Carli, C. Boehler, M. Asplund, D. Ricci, L. Fadiga, T. Stieglitz, *Biomaterials* **2020**, *255*, 120178.
[61] E. S. Boyden, F. Zhang, E. Bamberg, G. Nagel, K. Deisseroth, *Nat Neurosci* **2005**, *8*, 1263.

[62] C. M. Lewis, C. Boehler, R. Liljemalm, P. Fries, T. Stieglitz, M. Asplund, *Adv Healthcare Materials* **2024**, 2303401.
[63] T. B. Yasar, P. Gombkoto, A. L. Vyssotski, A. D. Vavladeli, C. M. Lewis, B. Wu, L. Meienberg, V. Lundegardh, F. Helmchen, W. Von Der Behrens, M. F. Yanik, *Nat Commun* **2024**, *15*, 4822.
[64] C. Böhler, M. Vomero, M. Soula, M. Vöröslakos, M. Porto Cruz, R. Liljemalm, G. Buzsaki, T. Stieglitz, M. Asplund, *Advanced Science* **2023**, *10*, 2207576.
[65] J. J. Nassi, M. C. Avery, A. H. Cetin, A. W. Roe, J. H. Reynolds, *Neuron* **2015**, *86*, 1504.
[66] A. Arieli, A. Grinvald, H. Slovin, *Journal of Neuroscience Methods* **2002**, *114*, 119.
[67] C. Hassler, T. Boretius, T. Stieglitz, *J Polym Sci B Polym Phys* **2011**, *49*, 18.
[68] D. H. Hubel, T. N. Wiesel, *The Journal of Physiology* **1962**, *160*, 106.
[69] R. J. Douglas, K. A. Martin, *The Journal of Physiology* **1991**, *440*, 735.
[70] R. J. Douglas, K. A. C. Martin, D. Whitteridge, *Neural Computation* **1989**, *1*, 480.
[71] B. R. Payne, *Cereb Cortex* **1993**, *3*, 1.
[72] U. Mitzdorf, *Physiological Reviews* **1985**, *65*, 37.
[73] A. L. Orsborn, C. Wang, K. Chiang, M. M. Maharbiz, J. Viventi, B. Pesaran, in *2015 7th International IEEE/EMBS Conference on Neural Engineering (NER)*, IEEE, Montpellier, France **2015**, pp. 398–401.
[74] A. Yazdan-Shahmorad, C. Diaz-Botia, T. L. Hanson, V. Kharazia, P. Ledochowitsch, M. M. Maharbiz, P. N. Sabes, *Neuron* **2016**, *89*, 927.
[75] N. M. Dotson, S. J. Hoffman, B. Goodell, C. M. Gray, *Neuron* **2017**, *96*, 769.
[76] K. Tybrandt, D. Khodagholy, B. Dielacher, F. Stauffer, A. F. Renz, G. Buzsáki, J. Vörös, *Advanced Materials* **2018**, *30*, 1706520.
[77] A. M. Packer, L. E. Russell, H. W. P. Dalgleish, M. Häusser, *Nat Methods* **2015**, *12*, 140.
[78] L. Carrillo-Reid, S. Han, W. Yang, A. Akrouh, R. Yuste, *Cell* **2019**, *178*, 447.
[79] J. H. Marshel, Y. S. Kim, T. A. Machado, S. Quirin, B. Benson, J. Kadmon, C. Raja, A. Chibukhchyan, C. Ramakrishnan, M. Inoue, J. C. Shane, D. J. McKnight, S. Yoshizawa, H. E. Kato, S. Ganguli, K. Deisseroth, *Science* **2019**, *365*, eaaw5202.
[80] G. Faini, D. Tanese, C. Molinier, C. Telliez, M. Hamdani, F. Blot, C. Tourain, V. De Sars, F. Del Bene, B. C. Forget, E. Ronzitti, V. Emiliani, *Nat Commun* **2023**, *14*, 1888.
[81] O. Sadakane, Y. Masamizu, A. Watakabe, S.-I. Terada, M. Ohtsuka, M. Takaji, H. Mizukami, K. Ozawa, H. Kawasaki, M. Matsuzaki, T. Yamamori, *Cell Reports* **2015**, *13*, 1989.
[82] A. K. Garg, P. Li, M. S. Rashid, E. M. Callaway, *Science* **2019**, *364*, 1275.
[83] M. Li, F. Liu, H. Jiang, T. S. Lee, S. Tang, *Neuron* **2017**, *93*, 1049.
[84] S. Xiao, W. J. Cunningham, K. Kondabolu, E. Lowet, M. V. Moya, R. A. Mount, C. Ravasio, E. Bortz, D. Shaw, M. N. Economo, X. Han, J. Mertz, *Nat Methods* **2024**, *21*, 1094.
[85] K. B. Clancy, I. Orsolic, T. D. Mrsic-Flogel, *Nat Neurosci* **2019**, *22*, 778.
[86] A. J. Peters, J. M. J. Fabre, N. A. Steinmetz, K. D. Harris, M. Carandini, *Nature* **2021**, *591*, 420.
[87] C. M. Lewis, J. Ni, T. Wunderle, P. Jendritza, A. Lazar, I. Diester, P. Fries, *Cell Reports* **2021**, *35*, 109083.
[88] L. Nurminen, S. Merlin, M. Bijanzadeh, F. Federer, A. Angelucci, *Nat Commun* **2018**, *9*, 2281.
[89] L. Collins, J. Francis, B. Emanuel, D. A. McCormick, *eLife* **2023**, *12*, e81826.
[90] V. Zerbi, A. Floriou-Servou, M. Markicevic, Y. Vermeiren, O. Sturman, M. Privitera, L. Von Ziegler, K. D. Ferrari, B. Weber, P. P. De Deyn, N. Wenderoth, J. Bohacek, *Neuron* **2019**, *103*, 702.
[91] M. Markicevic, B. D. Fulcher, C. Lewis, F. Helmchen, M. Rudin, V. Zerbi, N. Wenderoth, *Cerebral Cortex* **2020**, *30*, 4922.
[92] S. Lohani, A. H. Moberly, H. Benisty, B. Landa, M. Jing, Y. Li, M. J. Higley, J. A. Cardin, *Nat Neurosci* **2022**, *25*, 1706.
[93] D. Xiao, M. P. Vanni, C. C. Mitelut, A. W. Chan, J. M. LeDue, Y. Xie, A. C. Chen, N. V. Swindale, T. H. Murphy, *eLife* **2017**, *6*, e19976.
[94] Y. Huo, H. Chen, Z. V. Guo, *Neuron* **2020**, *107*, 1080.

[95] Z. V. Guo, N. Li, D. Huber, E. Ophir, D. Gutnisky, J. T. Ting, G. Feng, K. Svoboda, *Neuron* **2014**, *81*, 179.
[96] R. S. Snider, W. T. Niemer, *A Stereotaxic Atlas of the Cat Brain*, University of Chicago Press **1961**.
[97] G. Paxinos, *The marmoset brain in stereotaxic coordinates*, 1st ed., Academic Press, London **2012**.
[98] G. Paxinos, C. Watson, *The rat brain in stereotaxic coordinates*, 3. ed., Academic Press, San Diego, Calif. **1997**.
[99] D. H. Brainard, *Spatial Vis* **1997**, *10*, 433.